Hindawi
Advances in Meteorology
Volume 2019, Article ID 6253832, 13 pages
https://doi.org/10.1155/2019/6253832

Research Article

Based on the Gaussian Fitting Method to Derive Daily Evapotranspiration from Remotely Sensed Instantaneous Evapotranspiration

Suhua Liu,[1,2,3] **Hongbo Su**,[4] **Renhua Zhang**,[3] **Jing Tian**,[3] **Shaohui Chen**,[3] **Weimin Wang**,[5] **Lijun Yang**,[5] **and Hong Liang**[5]

[1]*School of Water Conservancy, North China University of Water Resources and Electric Power, Zhengzhou 450046, China*
[2]*Henan Key Laboratory of Water Environment Simulation and Treatment, Zhengzhou 450046, China*
[3]*Key Laboratory of Water Cycle & Related Land Surface Processes, Institute of Geographic Sciences and Natural Resources Research, Chinese Academy of Sciences, Beijing 100101, China*
[4]*Department of Civil, Environmental and Geomatics Engineering, Florida Atlantic University, Florida, FL 33431, USA*
[5]*Shenzhen Environmental Monitoring Center, Shenzhen 518049, China*

Correspondence should be addressed to Hongbo Su; hongbo@ieee.org and Jing Tian; tianj.04b@igsnrr.ac.cn

Received 21 April 2018; Accepted 3 December 2018; Published 14 January 2019

Academic Editor: James Cleverly

Evapotranspiration (ET) is a significant component in the water cycle, and the estimation of it is imperative in water resource management. Regional ET can be derived by using remote sensing technology which combines remote sensing inputs with ground-based measurements. However, instantaneous ET values estimated through remote sensing directly need to be converted into daily totals. In this study, we attempted to retrieve daily ET from remotely sensed instantaneous ET. The study found that the Gaussian fitting curve closely followed the ET measurements during the daytime and hence put forward the Gaussian fitting method to convert the remotely sensed instantaneous ET into daily ETs. The method was applied to the middle reaches of Heihe River in China. Daily ETs on four days were derived and evaluated with ET measurements from the eddy covariance (EC) system. The correlation between daily ET estimates and measurements showed high accuracy, with a coefficient of determination (R^2) of 0.82, a mean average error (MAE) of 0.41 mm, and a root mean square error (RMSE) of 0.46 mm. To make more scientific assessments, percent errors were calculated on the estimation accuracy, which ranged from 0% to 18%, with more than 80% of locations having the percent errors within 10%. Analyses on the relationship between daily ET estimates and land use status were also made to assess the Gaussian fitting method, and the results showed that the spatial distribution of daily ET estimates well demonstrated ET differences caused by land use types and was intimately linked with the vegetation pattern. The comparison between the Gaussian fitting method and the sine function method and the ETrF method indicated that results derived through the Gaussian fitting method had higher precision than that obtained by the sine function method and the ETrF method.

1. Introduction

Evapotranspiration (ET), which is crucial to the hydrological cycle, is defined as the synthesis process of evaporation and transpiration. It is the link of energy and water exchanges among the biosphere, atmosphere, and hydrosphere [1–5]. In most cases, ET is the largest loss of precipitation, and it is a significant outgoing water flux from the earth's surface. In semiarid areas, the amount of ET almost equals that of precipitation [6]. Hence, accurate estimation of ET is beneficial to improve applications in many fields, such as drought mitigation strategies, irrigation system performance, optimization of irrigation water use, hydrological modeling, and accurate initialization of climate prediction models, and is also very useful for understanding the global climate change, the local to global energy and water cycles, ecosystem processes, and land-atmosphere interaction [7–12]. Ground-based observations including Bowen ratio

tower, eddy covariance [13], lysimeter, and large aperture scintillometer can provide ET measurements with some advantages. However, regional ET acquired through these methods is time-consuming and labour-intensive because it requires numerous installations and considerable spatial interpolations [8].

Satellite remote sensing makes it possible for acquiring regional ET over various spatial scales, ranging from individual pixels to an entire raster image that may cover a whole river basin [14]. In the last two decades, the recent advances of remote sensing technology together with the requirement for quantifying regional ET have brought about numerous researches in obtaining large-scale ET [8, 10, 15, 16]. Remote sensing can retrieve an instantaneous ET on a regional scale at the time of satellite overpass. However, daily ET estimates are required for water resources monitoring and ecological management purposes [14, 17]. Consequently, it is of significance to convert instantaneous ET into daily ET [18, 19].

Several instantaneous ET extrapolation methods are proposed and developed to derive daily ET, such as the sine function method [20], the evaporative fraction (EF) method [21], and the reference ET fraction (ETrF) method [22]. Jackson et al. [20] proposed a technique based on the ratio of daily solar radiation to instantaneous solar radiation. Given it was similar to that of solar irradiance throughout the daylight period, they assumed the generic trend for the ET diurnal course could be approximated by a sine function which is named the sine function method. Zhang and Lemeur [23] did researches on the sine function method, and they concluded that the sine function method was preferable to estimate daily ET using remote sensing data. The disadvantage of this method is that it is limited by its empirical nature in applications [14]. The EF, defined as the latent heat flux divided by the latent heat flux plus sensible heat flux (available energy (AE)), is nearly constant during the daytime period [24, 25]. Hence, the method can utilize instantaneous EF and continuous measurements of the available energy flux to determine daily ET. Studies [23] showed that the assumption of a constant EF was valid under cloud-free conditions. Sugita and Brutsaert [26] also yielded accurate estimates of daily ET by the EF method. However, some studies found that EF changes with the available energy, surface resistance, and other environmental variables, which caused uncertainties in applying the EF method [23]. Tasumi et al. [27] investigated a method labeled "reference ET fraction," which was defined as the ratio of actual ET to reference ET (ETr) for an alfalfa crop. This method assumes that the instantaneous ETrF is similar to the daily average ETrF. Many studies have been conducted to utilize the ETrF method to derive daily ET, and the results show that the ETrF remains constant during the daytime [28]. The ETrF method, however, seems to perform well under homogeneous surface conditions [29].

The aforementioned instantaneous ET extrapolation methods request numerous variables, and some of the variables may be difficult to attain through remote sensing. For example, the EF method needs an instantaneous EF value and daytime total available energy, the sine function method requests several variables related to geographic location, and the ETrF method demands variables linked with specific crops. To simplify the computation process of daily ET, the study put forward a method of deriving daily ET, which was based on the ET diurnal course and similar to the sine function method. In this paper, we assume that, for clear sky days, the diurnal course of solar radiation and ET can be adequately expressed by the Gaussian fitting curve and then develop the Gaussian fitting approach for calculating daily ET from instantaneous ET. Section 2 includes two subsections: Section 2.1 presents a description on the theory of retrieving instantaneous ET by remote sensing and Section 2.2 introduces the Gaussian fitting method for deriving daily ET. Section 3 describes the datasets and the study area used to assess the Gaussian fitting method. Section 4 shows the results. Section 5 provides discussions on the advantages and limitations of the Gaussian fitting method, and Section 6 summarizes a conclusion of the work.

2. Methodology

2.1. Obtaining the Instantaneous ET. In the study, we adopted the energy balance theory to compute the instantaneous ET. Without considering the energy transported by horizontal advection and consumed by photosynthesis, the energy exchanged between the land surface and the atmosphere can be described by the energy balance equation:

$$\mathrm{LE} = R_n - H - G, \tag{1}$$

where R_n, H, LE, and G are the net radiation, sensible heat flux, latent heat flux, and soil heat flux, respectively. Units of the four items are W/m^2. In equation (1), net radiation, R_n, sensible heat flux, H, and soil heat flux, G, can be determined by the following equations, respectively:

$$R_n = S_0(1-\alpha) + R_{ld} - \sigma\varepsilon_s T_0^4, \tag{2}$$

$$H = \frac{\rho C_p}{r_a}(T_0 - T_a), \tag{3}$$

$$G = 0.3(1 - 0.9 f_v) R_n, \tag{4}$$

where S_0 (W/m^2) is the downward shortwave radiation, α is the surface albedo, R_{ld} (W/m^2) is the downward longwave radiation, σ is the Stefan–Boltzmann constant and the value of it is 5.67×10^{-8} W·m^{-2}·K^{-4}, ε_s is the surface emissivity, T_0 (K) is the aerodynamic temperature and is usually substituted with land surface temperature (LST) in applications [30, 31], ρ is the air density, C_p (1004 J/(kg·K)) is the specific heat at constant pressure of air, and r_a (s/m) is the air aerodynamic resistance and can be calculated by the classical formulae that take into account the stability correction functions for temperature and wind. Readers can refer to the calculation process of r_a by Abdelghani et al. [32]. T_a (K) is the surface air temperature, and f_v is the fractional vegetation cover which was calculated using NDVI images, with NDVI_{min} of the bare soil and NDVI_{max} of dense vegetation. The formula is as follows [33]:

$$f_v = \left(\frac{\mathrm{NDVI} - \mathrm{NDVI}_{\min}}{\mathrm{NDVI}_{\max} - \mathrm{NDVI}_{\min}}\right)^2, \quad (5)$$

where NDVI is the ratio of the differences in reflectivity between the near-infrared (NIR) band and the red (R) band to their sum:

$$\mathrm{NDVI} = \frac{\rho_{\mathrm{NIR}} - \rho_{\mathrm{R}}}{\rho_{\mathrm{NIR}} + \rho_{\mathrm{R}}}, \quad (6)$$

where ρ_{NIR} and ρ_{R} are the reflectivities for near-infrared and red bands, respectively.

The latent heat flux, LE, can be acquired as the following equation by integrating equations (1)–(4):

$$\begin{aligned}\mathrm{LE} = {} & (1-\alpha)S_0 + R_{\mathrm{ld}} - \varepsilon_s \sigma \mathrm{LST}^4 - \frac{\rho C_p}{r_a}\left(\mathrm{LST} - T_a\right) \\ & - 0.3\left(1 - 0.9 f_v\right)\left(S_0(1-\alpha) + R_{\mathrm{ld}} - \sigma\varepsilon_s T_0^4\right),\end{aligned} \quad (7)$$

where variables including α, ε_s, LST, and f_v can be calculated through remote sensing images, r_a is attained by referring to Abdelghani et al. [32], and variables including S_0, R_{ld}, and T_a are acquired from the meteorological stations.

2.2. Obtaining the Daily ET. Jackson et al. put forward the assumption that the diurnal course of ET was similar to that of solar irradiance and could be approximated by a sine function [20, 23]. The attempt provided in our study is also an approximation similar to the sine function method, which is named the Gaussian fitting method.

According to our observations, we found that not only the diurnal course of net radiation but also the diurnal course of ET during the daytime can be approximated by the Gaussian fitting curve [34]. Hence, we applied the Gaussian fitting curve to fit the diurnal course of ET on several clear sky days. A comparison between ET measurements at EC stations and ET estimates by the Gaussian fitting curve is shown in Figure 1. The points represent the values of net radiation measurements observed every 10 minutes (Figure 1(a)) and ET measurements observed every 30 minutes (Figure 1(b)) throughout the day, respectively. The lines represent the best fits of Gaussian fitting curves to the experimental data. It is obvious that the Gaussian fitting curves closely follow the experimental data during the daytime (from sunrise to sunset).

The Gaussian fitting function can be expressed as follows:

$$y = y_0 + \frac{A}{w\sqrt{\pi/2}} e^{-2\left((x-x_c)^2/w^2\right)}. \quad (8)$$

To explain the meanings of the variables in equation (8), we display a Gaussian fitting curve to help the description (Figure 2). Combining equation (8) with Figure 2, the variables in equation (8) are illustrated clearly: y_0 is the offset; x_c is the center where y has $y_{\max}$, y_c is the maximum value when $x = x_c$, and $y_{\max}$ is equal to y_c; (x_c, y_c) is the extreme value point; w is the width that equals 2δ, in which δ is the standard deviation of y; and A is the area of the curve. Comparing the diurnal course of latent heat flux with equation (8), we can rewrite equation (8) and attain the similar formula for expressing the diurnal course of ET, as follows:

$$\mathrm{ET}_i = \mathrm{ET}_0 + \frac{A}{w\sqrt{\pi/2}} e^{-2\left((t_i - t_c)^2/w^2\right)}, \quad (9)$$

where ET_i is the instantaneous ET at the moment of the satellite overpass, ET_0 is the value at sunset or sunrise (usually equals zero), t_i is the time of the satellite overpass, and t_c is the time when the instantaneous ET arrives at its daily maximum. To acquire the daily ET, we need to calculate the integral of equation (9), which would be a complex process. Fortunately, we notice that the variable A is the area of the curve (equation (9)) and is the approximate integration of instantaneous ET. Hence, the daily ET can be attained as follows:

$$\mathrm{ET}_d = A = w\sqrt{\frac{\pi}{2}} \times \mathrm{ET}_i \times e^{2\left((t_i - t_c)^2/w^2\right)}. \quad (10)$$

From formula derivation above, we know that the unique advantage of the Gaussian fitting method is that the expression of Gaussian fitting equation has already contained the daily ET. In equation (10), if ASTER satellite data, which pass the western China at about 12 : 15 pm, are used, then t_i equals 12.25 (h), and t_c is the time when the instantaneous ET arrives at its daily maximum and is usually set to 14.5 (h).

As for w, we adopted an empirical value that was equal to half of the time, during which net radiation is greater than zero ($t_{R_n>0}$). The following are the justifications on the determination of w.

To find out the relationship between $t_{R_n>0}$ and w, we utilized one-month measurements of net radiation and ET (except cloudy days) at four EC stations with different underlying surfaces (Table 1). $t_{R_n>0}$ is determined by net radiation measurements and w is calculated by making Gaussian fitting on ET observations. Figure 3 gives the linear fitting results between $t_{R_n>0}/2$ and w. It reveals that the relationship of $t_{R_n>0}/2$ and w is close to the 1 : 1 line. As a result, w can be approximated as $t_{R_n>0}/2$.

3. Study Area and Datasets

3.1. Study Area. Belonging to the middle basin of the second longest inland river of China, Heihe River, the study area is located in Zhangye Oasis, Gansu, China, with the latitude of 38.83°N~38.93°N and the longitude of 100.32°E~100.42°E, as shown in Figure 4. Because of being landlocked, it is obviously characterized by an arid climate with a low annual mean rainfall of 124.9 mm, a high potential evaporation of more than 2000 mm, a large temperature difference between day and night, and long hours of sunshine. The study region is covered with maize, orchard, vegetable, woodland, and built-up areas (villages). From May to September, the staple crops in the study region are seed corns, fruit trees, and vegetables.

For retrieving the daily ET, remote sensing data, such as ASTER images and HJ-1 A/B images, together with ground-based measurements including meteorological variables and surface fluxes are utilized.

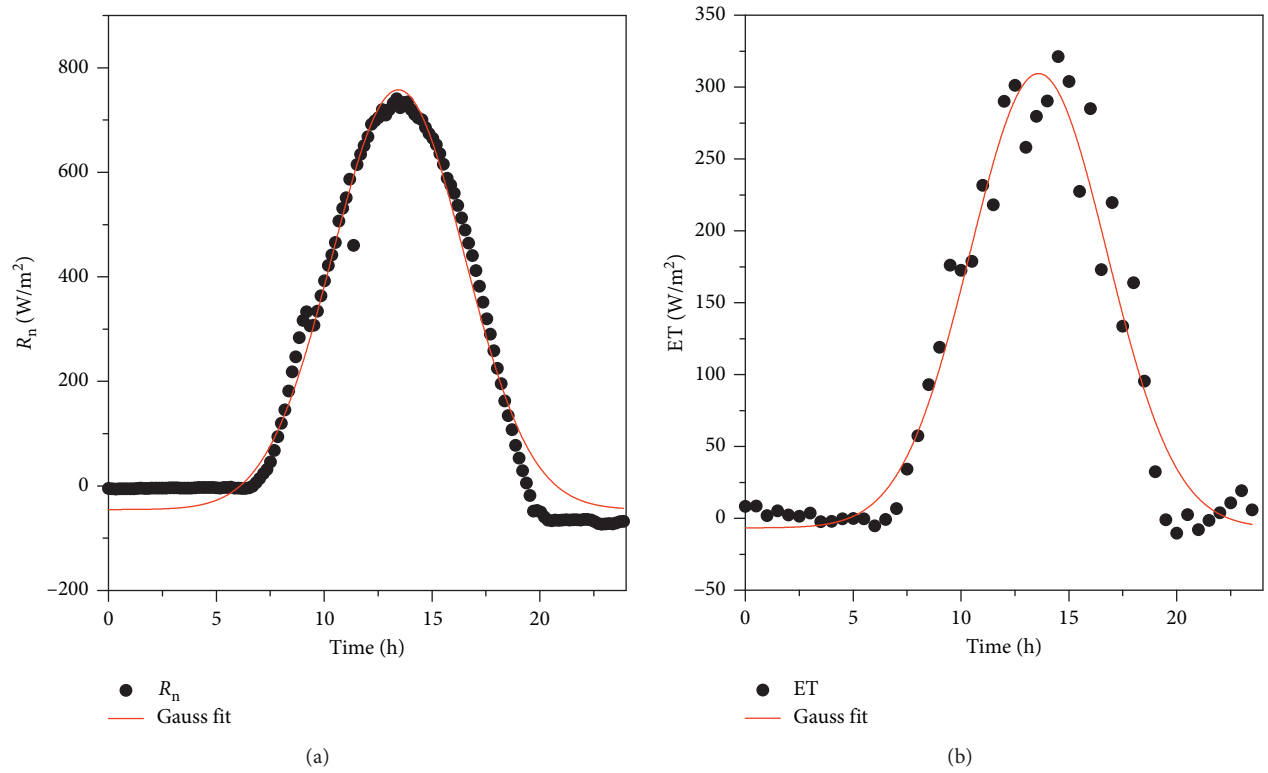

Figure 1: Diurnal course of solar radiation (a) and latent heat flux (b) at middle reaches of Heihe River for a clear sky day: August 14, 2012. Symbols represent experimental data. The lines were calculated from the Gaussian fitting function.

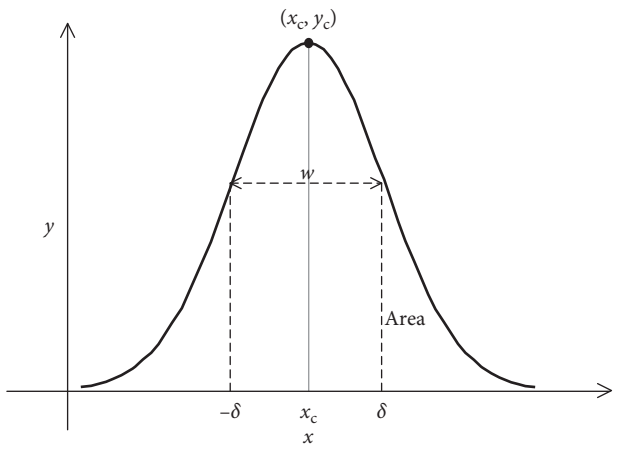

Figure 2: A Gaussian fitting curve of equation (8).

Table 1: Details on EC stations used for validity verification.

Name	EC1	EC4	EC10	EC17
The underlying surface	Vegetable	Village	Maize	Orchard
Days to test the validity	9 days	12 days	12 days	12 days

3.2. Remote Sensing Data. ASTER is a sensor that acquires numerous images in different bands including multispectral visible, near-infrared, and thermal infrared. It is intended to monitor climate, land surface energy balance, and hydrological processes [35]. In the study, the vegetation fraction

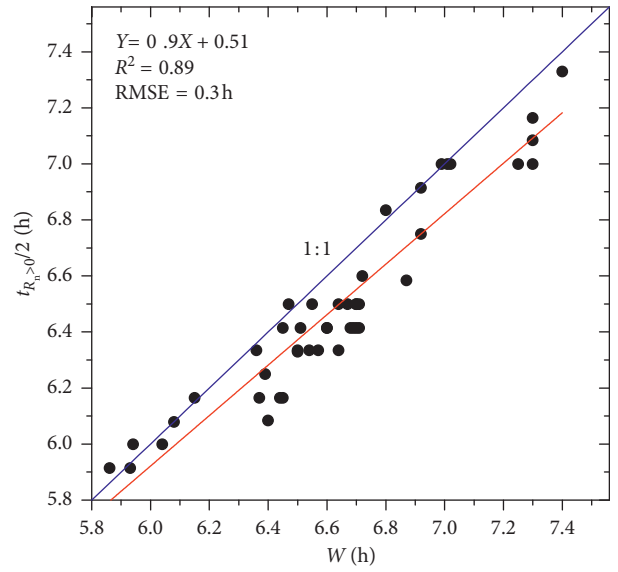

Figure 3: The relationship between w and $t_{R_n>0}$.

and the surface emissivity were estimated through ASTER images in the visible and near-infrared wave bands (0.52~0.86 μm), which had a high spatial resolution of 15 m. As for the variable of LST, the study utilized products provided by the Heihe Plan Science Data Center [36, 37], which were retrieved from the thermal infrared wave band (8.125~11.65 μm) of ASTER images, with a spatial resolution of 90 m. The albedo, which is another imperative variable,

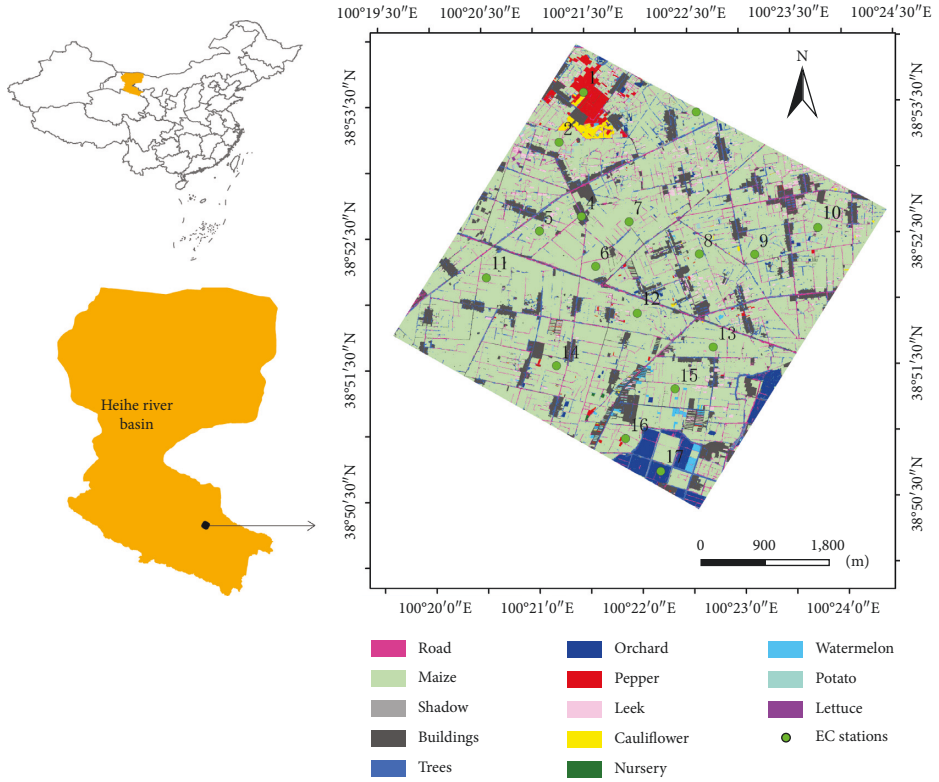

Figure 4: Location of the study area with land use types and 17 stations.

was obtained from HJ-1 A/B images. HJ-1 A/B, which was launched by China in 2008, is a small satellite constellation primarily applied to forecasting and monitoring environmental disasters and changes. Each satellite of the satellite constellation carries two CCDs (0.45~0.89 μm) that can acquire images with a spatial resolution of 30. HJ-1 A/B revisits the same place every 3 or 4 days.

3.3. Ground Observations. Ground-based observations were provided by Heihe Watershed Allied Telemetry Experimental Research (HiWATER), which was an ecohydrological and watershed-scale experiment. From an interdisciplinary perspective, the HiWATER experiment was designed to address studies including uncertainty, scaling, heterogeneity, and closing of the water cycle in the watershed scale [13, 38], and the experiment was conducted between May and September 2012 and involved an observation matrix. The study area of the experiment was the Heihe River Basin. Users can access the data through Cold and Arid Regions Science Data Center at Lanzhou (http://westdc.westgis.ac.cn/).

There are 17 elementary sampling plots (as shown in Figure 4) equipped with EC stations and automatic meteorological stations. The 17 elementary sampling plots were divided according to the distribution of crops, shelterbelts, residential areas, roads, and canals, as well as according to soil moisture and irrigation status [39].

Original EC measurements were collected at a sampling frequency of 10 Hz. The processing work on EC data includes spike detection, lag correction of H_2O/CO_2 relative to the vertical wind component, sonic virtual temperature correction, coordinating rotation using the planar fit method, corrections for density fluctuation (WPL correction), and frequency response correction. The post-processing software named "EdiRe" was utilized to make the above corrections (University of Edinburgh; http://www.geos.ed.ac.uk/abs/research/micromet/EdiRe) [40, 41]. Besides the corrections made by the EdiRe software, the half-hourly flux data are screened based on four criteria: (1) data are rejected when the sensor is malfunctioning (e.g., when there is a fault diagnostic signal), (2) data are rejected when precipitation occurs within 1 h before and after the collection, (3) incomplete 30 min data are rejected when the missing ratio is larger than 3% in the 30 min raw record, and (4) data are rejected at night when the friction velocity is below 0.1 m/s [13].

The automatic meteorological stations can monitor meteorological variables, such as solar radiation, wind speed, wind direction, air pressure, air temperature, and air humidity, with the sample intervals of 10 minutes and 1 minute. The EC stations can acquire surface fluxes including latent heat flux and sensible heat flux with a sample interval of 30 minutes [42].

4. Results

4.1. Validity Verification. To test the validity of the Gaussian fitting method, we utilized the Gauss fitting curve to simulate the diurnal variation of instantaneous ET observed at EC stations with different underlying surfaces. Table 1 gives

descriptions of EC stations used for making the validity verification.

To make the validity verification more persuasive, we used the whole EC data in June, except that on cloudy, rainy, and data missing days, from four sites (EC1, EC4, EC10, and EC17) to make the Gaussian fitting analysis. Figure 5 gives the Gaussian fitting results on ET measurements on nine days in June 2012 at EC 1. Similarly, fitting analyses for ET measurements on twelve days in June 2012 at EC4, EC10, and EC17 were also carried on from the aspects of the fitting equation, the coefficients of determination (R^2), and the root mean square errors (RMSEs), and the results were summarized and displayed in table forms, as shown in Tables 2–4, respectively. For EC1 with the vegetable surface, the R^2 between the simulations by the Gaussian fitting method and the measurements are higher than 0.9 on most days and the RMSEs are lower than 20 W/m^2 on all days. For EC4, EC10, and EC17 with village, maize, and orchard surfaces, respectively, the R^2 are higher than 0.84 and the RMSEs are lower than 20 W/m^2. Previous studies [16] showed an RMSE of about 20–45 W/m^2 on diurnal ET estimates. Therefore, our results are satisfactory. According to the above results, it is obvious that the Gaussian fitting results in June 2012 are quite consistent with the diurnal variation of ET measurements at EC stations, no matter the underlying surface, which means the Gaussian fitting method can describe the diurnal variation of ET accurately and can be used as an approach to simulate daily ET.

4.2. Evaluating Daily ET Estimates Derived by the Gaussian Fitting Method. Four clear sky days, June 24, July 10, and August 11 and 27, 2012, were utilized to calculate the daily ET by the Gaussian fitting method. As mentioned in Section 3.1, remote sensing data (ASTER images and HJ-1 A/B images) with ground-based measurements were combined to retrieve instantaneous ET on the four days, and then, the retrieved instantaneous ET was inputted into the Gaussian fitting method to derive daily ET. The spatially distributed daily ETs on the four days are shown in Figure 6. To evaluate the daily ET estimates by the Gaussian fitting method, analyses in four aspects that are results validation, error analysis, the relationship between daily ET estimates and the land use status, and the comparison between the Gaussian fitting method and the sine function method were performed.

4.2.1. Validating Daily ET Estimates. Daily ET estimates derived by the Gaussian fitting method for the four days are tested against ET measurements (68 points) at ground-based EC stations (Figure 7). An R^2 of 0.82, an MAE of 0.41 mm, and an RMSE of 0.46 mm were obtained. Almost all the points had absolute errors lower than 1 mm and 69% of the points had absolute errors lower than 0.5 mm. The correlation analysis stated that the retrieved daily ET estimates were quite consistent with the ground-based observations, which means that daily ET estimates by the Gaussian fitting method were close to the 1 : 1 line and had high accuracy.

4.2.2. Error Analyses. The study made error analyses from two aspects, one is the percent error and the other is the relationship between errors and land use.

According to the error analysis and the numerical analysis theory, the percent error is more scientific and more robust than the absolute error for assessing the accuracy of estimates [43]. Therefore, the frequency distribution of the percent errors was conducted. The definition of the percent error is the absolute error divided by the magnitude of the exact value. Its expression is

$$\delta = \frac{\Delta}{L} \times 100\%, \tag{11}$$

where Δ is the absolute error, δ is the percent error, and L is the exact value.

Figure 8 shows the frequency distribution of the percent errors on daily ET estimates, which had a variation from 0% to 18%. An accuracy of the percent errors within 10% was achieved at more than 80% of locations, and the other 20% of locations had the percent errors between 10% and 18%. The results demonstrated that the Gaussian fitting method had high estimation accuracy.

As for the relationship between errors and land uses, we utilized estimations from land covers of vegetable, village, maize, and orchard and their corresponding ground-based observations that were at the site of EC1, EC4, EC10, and EC17 on June 24, July 10, and August 11 and 27, 2012, to calculate and analyze the estimation errors. To avoid abnormal variation, the study used the average values of observations and estimations for four days to analyze, and the results are shown in Table 5. The land cover of village (EC4) had the maximum estimation error, whereas the other three land cover types, the vegetable, the maize, and the orchard, had minor estimation error, which was concordant with the conclusions of Section 4.1 that the Gaussian fitting effects at EC4 were less effective than those at the other three sites. The estimation error analyses indicated that the Gaussian fitting method had higher precision on underlying surfaces covered with vegetation than on bare areas.

4.2.3. Relationship between ET Estimates and Land Use. Previous studies suggested that the spatial distribution of ET was strongly related to land cover types and that studies on ET estimates at a regional scale always required the incorporation of heterogeneous surface status [44]. Hence, the relationship between ET estimates and land use status can illustrate the rationality of ET estimates in some degree. The land use maps (Figure 4) provided by Heihe Plan Science Data Center [45] were derived from the CASI (aerial remote sensing data of Compact Airborne Spectrographic Imager) and adopted the SVM (support vector machine) as the classification method. Comparing the spatial distribution of daily ET estimates (Figure 6) with the land use status (Figure 4), it is obvious that ET estimates linked with the land use type well; that is, built-up areas (village) displayed low ET values, and dense vegetation areas (maize and orchard) showed high ET values.

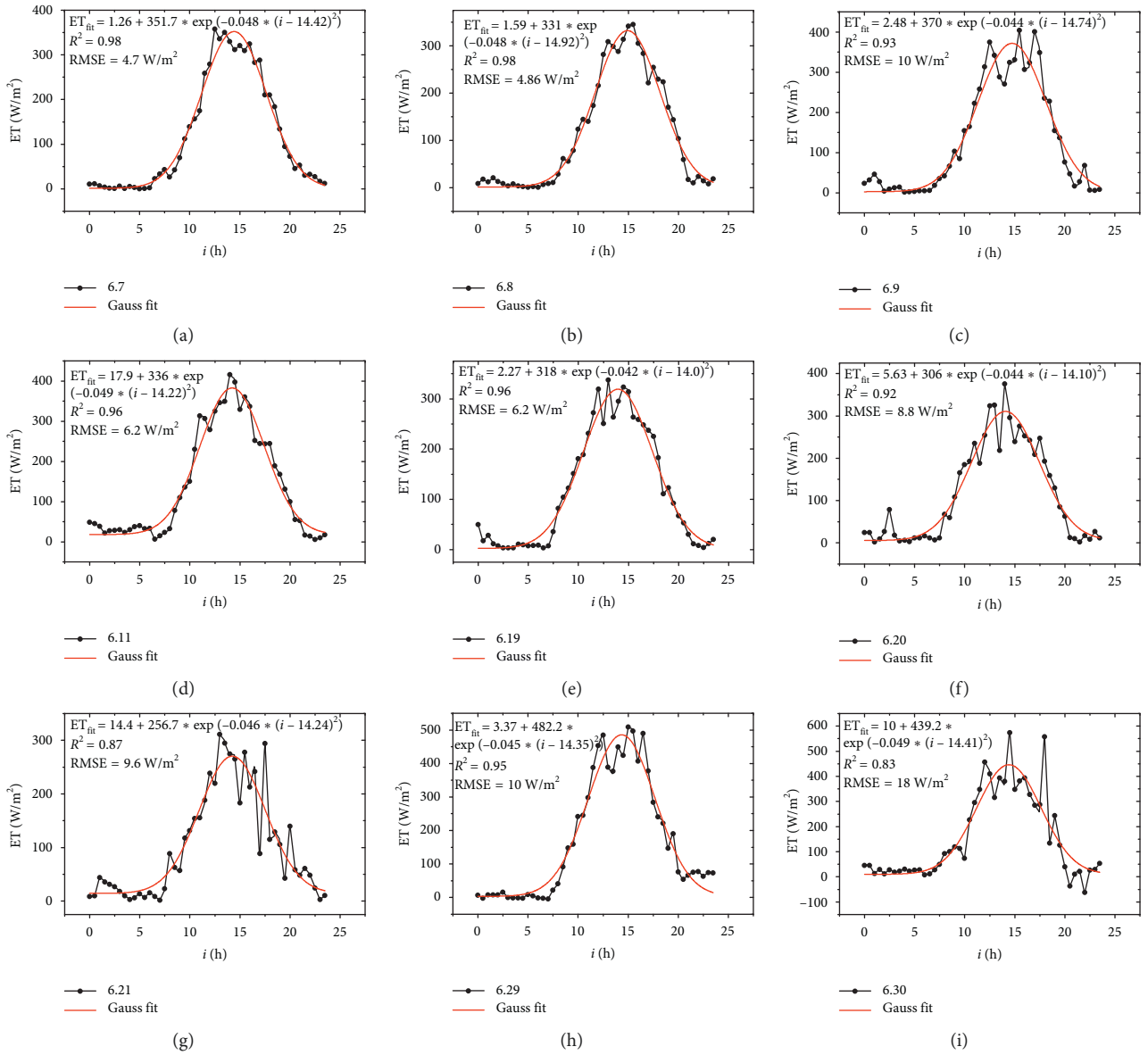

Figure 5: Gaussian fitting results on ET measurements at EC1 on cloud-free days in June 2012.

Table 2: Gaussian fitting results on ET measurements at EC4 on cloud-free days in June 2012.

Date	Fitting equation	R^2	RMSE (W/m^2)
June 7	$ET_{fit} = 3.81 + 216.4 * \exp(-0.044 * (i - 13.6)^2)$	0.90	7
June 8	$ET_{fit} = -2.9 + 162.5 * \exp(-0.034 * (i - 13.7)^2)$	0.85	8
June 9	$ET_{fit} = -4.48 + 158.7 * \exp(-0.038 * (i - 14.52)^2)$	0.87	6.5
June 11	$ET_{fit} = 5.9 + 156.6 * \exp(-0.043 * (i - 14.67)^2)$	0.92	4.5
June 15	$ET_{fit} = 0.1 + 148.8 * \exp(-0.041 * (i - 14.20)^2)$	0.91	4.6
June 16	$ET_{fit} = 0.7 + 153.4 * \exp(-0.037 * (i - 14.39)^2)$	0.89	5.69
June 19	$ET_{fit} = -2.9 + 165 * \exp(-0.038 * (i - 14.30)^2)$	0.87	7
June 20	$ET_{fit} = 10.56 + 136.2 * \exp(-0.037 * (i - 14.06)^2)$	0.97	5.8
June 21	$ET_{fit} = 4.85 + 144.8 * \exp(-0.041 * (i - 14.17)^2)$	0.87	5.7
June 24	$ET_{fit} = 1.88 + 193 * \exp(-0.045 * (i - 15.01)^2)$	0.84	7.9
June 29	$ET_{fit} = 4.5 + 255.2 * \exp(-0.036 * (i - 14.18)^2)$	0.94	7.3
June 30	$ET_{fit} = 6.6 + 204.4 * \exp(-0.037 * (i - 14.90)^2)$	0.86	8.7

Table 3: Gaussian fitting results on ET measurements at EC10 on cloud-free days in June 2012.

Date	Fitting equation	R^2	RMSE (W/m^2)
June 7	$ET_{fit} = -5.9 + 435.5 * \exp(-0.047 * (i - 13.65)^2)$	0.95	9.4
June 8	$ET_{fit} = -8.6 + 353.3 * \exp(-0.040 * (i - 14.10)^2)$	0.95	8.7
June 9	$ET_{fit} = -1.87 + 269.7 * \exp(-0.045 * (i - 13.94)^2)$	0.95	8.3
June 11	$ET_{fit} = 1.10 + 409.9 * \exp(-0.047 * (i - 13.96)^2)$	0.95	8.7
June 15	$ET_{fit} = -7.1 + 432.6 * \exp(-0.048 * (i - 14)^2)$	0.96	7.7
June 16	$ET_{fit} = -4.52 + 441.3 * \exp(-0.044 * (i - 14.16)^2)$	0.97	8
June 19	$ET_{fit} = -1.88 + 519.8 * \exp(-0.042 * (i - 14.0)^2)$	0.96	11
June 20	$ET_{fit} = -2.48 + 698.6 * \exp(-0.055 * (i - 14.27)^2)$	0.97	9.8
June 21	$ET_{fit} = 14.1 + 676.2 * \exp(-0.057 * (i - 13.88)^2)$	0.93	16
June 24	$ET_{fit} = -2.85 + 731.4 * \exp(-0.058 * (i - 14.0)^2)$	0.94	15.5
June 29	$ET_{fit} = 5.6 + 627.5 * \exp(-0.053 * (i - 14.28)^2)$	0.96	11
June 30	$ET_{fit} = 9.8 + 593 * \exp(-0.054 * (i - 14.052)^2)$	0.91	16.5

Table 4: Gaussian fitting results on ET measurements at EC17 on cloud-free days in June 2012.

Date	Fitting equation	R^2	RMSE (W/m^2)
June 7	$ET_{fit} = 6.7 + 437.6 * \exp(-0.049 * (i - 13.56)^2)$	0.92	12
June 8	$ET_{fit} = -4.89 + 423.2 * \exp(-0.045 * (i - 14.132)^2)$	0.92	12
June 9	$ET_{fit} = 4 + 454.5 * \exp(-0.057 * (i - 14.16)^2)$	0.94	9.6
June 11	$ET_{fit} = 2.2 + 439.5 * \exp(-0.045 * (i - 14.10)^2)$	0.93	11.5
June 15	$ET_{fit} = 0.68 + 342.2 * \exp(-0.045 * (i - 14.30)^2)$	0.94	8.7
June 16	$ET_{fit} = 4.8 + 367.2 * \exp(-0.044 * (i - 14.20)^2)$	0.93	10
June 19	$ET_{fit} = -14 + 414.7 * \exp(0.042 * (i - 13.42)^2)$	0.93	12
June 20	$ET_{fit} = -12 + 418.2 * \exp(-0.047 * (i - 14.10)^2)$	0.92	12
June 21	$ET_{fit} = 1.96 + 473 * \exp(-0.066 * (i - 13.56)^2)$	0.92	12
June 24	$ET_{fit} = -11 + 443.8 * \exp(-0.049 * (i - 13.962)^2)$	0.95	9
June 29	$ET_{fit} = -1.1 + 489.1 * \exp(-0.043 * (i - 14.2)^2)$	0.88	17.5
June 30	$ET_{fit} = -4.1 + 517.7 * \exp(-0.047 * (i - 14.562)^2)$	0.93	13

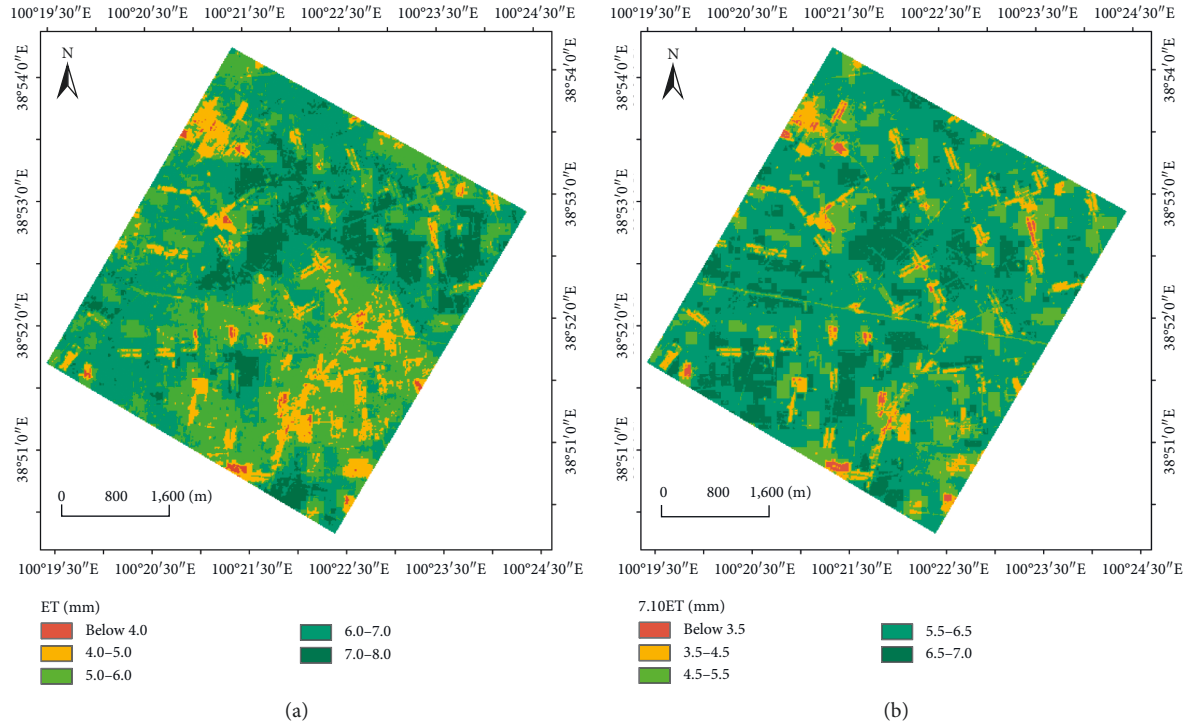

(a) (b)

Figure 6: Continued.

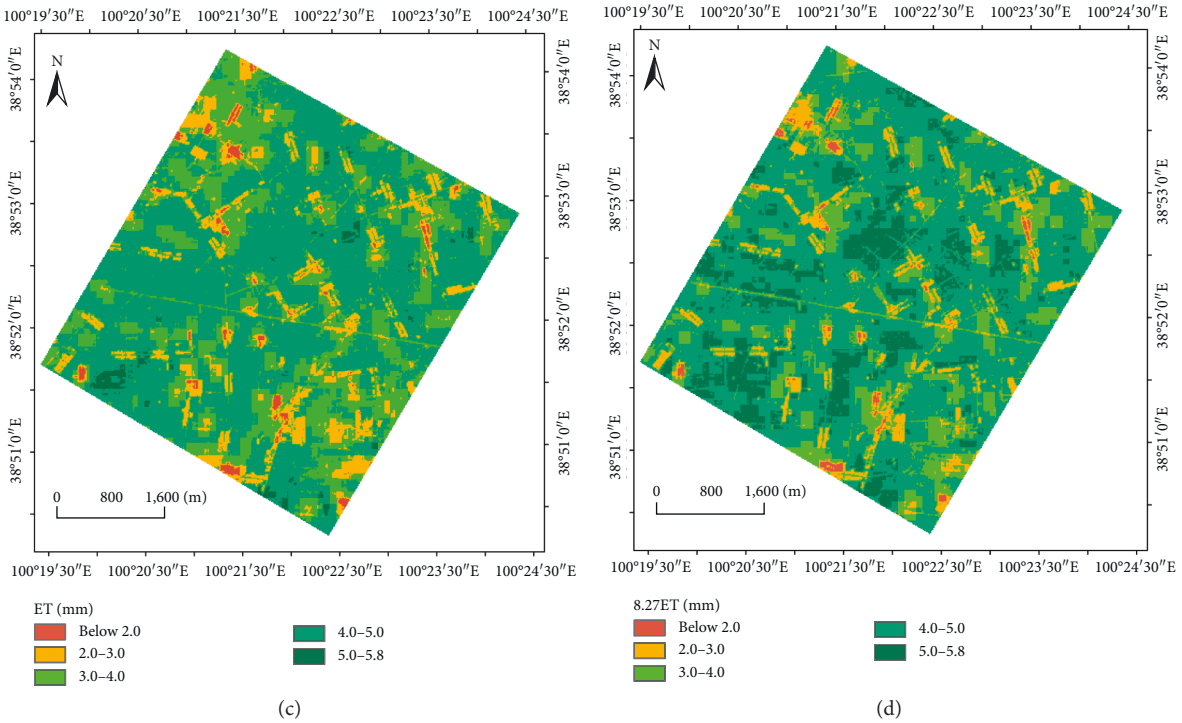

Figure 6: Daily ET calculated by the Gaussian fitting method on June 24 (a), July 10 (b), and August 11 (c) and 27 (d), 2012.

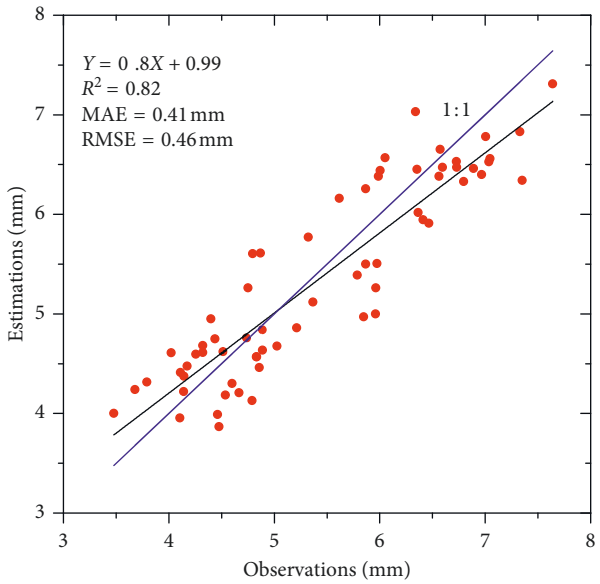

Figure 7: Comparison between daily observed ET by EC stations and that estimated by the Gaussian fitting method.

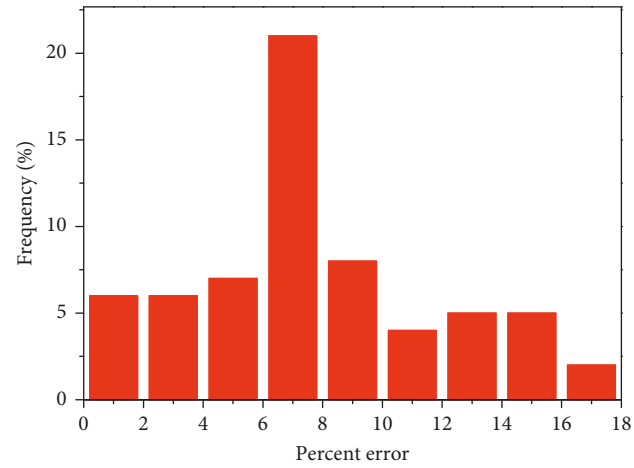

Figure 8: The frequency distribution of percent errors on daily ET estimates obtained by the Gaussian fitting method.

Table 5: Estimation errors at the site of EC1 EC4, EC10, and EC17.

Site	Observation (mm)	Estimation (mm)	Estimation error (mm)
EC1	5.3	4.7	−0.6
EC4	2.2	3.1	0.9
EC10	5.8	5.4	−0.4
EC17	4.9	5.2	0.3

The statistical work was done to make the analyses quantitatively. In the study area, there were four main land use types including maize, vegetable, orchard, and village. For each land use type, average daily ET on the four days was computed (Table 6). Clearly, maize and orchard had the maximum values. Maize had the average daily ET of 6.6 mm, 6.1 mm, 4.2 mm, and 4.6 mm on the four days, respectively; orchard had that of 6.8 mm, 5.9 mm, 4.3 mm, and 5.1 mm on the four days, respectively. Average daily ET for the vegetable was 5.3 mm and 4.7 mm on June 24 and July 10, respectively, and was around 3.5 mm on the other two days. Village areas

Table 6: Daily ET estimates derived by the Gaussian fitting method of the four different land use types on June 24, July 10, and August 11 and 27, 2012.

Land use type	June 24	July 10	August 11	August 27
Maize (mm)	6.6	6.1	4.2	4.6
Vegetable (mm)	5.3	4.7	3.5	3.6
Orchard (mm)	6.8	5.9	4.3	5.1
Village (mm)	4.0	3.6	2.2	2.4

displayed the lowest daily ET, with an average value of around 4 mm on June 24 and July 10 and no more than 2.5 mm on the other two days.

The spatial distribution of daily ET was strongly connected with the land cover. In June, July, and August, maize and fruit trees were in the vigorous growth season and with frequent irrigation. As a result, the vegetation cover was dense and the daily ET was high. Compared with maize and orchard, vegetables including pepper, leek, and cauliflower had a sparse vegetation cover during this time, and therefore, their daily ET values were lower than those of maize and orchard. Since villages were covered with buildings and the underlying surfaces were largely bare and solidified, the daily ET values over villages were the lowest.

Generally, high daily ET always agrees with a dense vegetation cover and low daily ET is usually in accordance with a sparse vegetation cover, which indicates that the daily ET results obtained by the Gaussian fitting method are consistent with the objective knowledge and can well perform the daily ET differences brought about by land use status.

4.2.4. The Comparisons between the Gaussian Fitting Method and the Sine Function Method and the ETrF Method. Similar to the sine function method, the Gaussian fitting method is also based on the diurnal variation of ET; hence, this section gives the comparisons between the Gaussian fitting method and the sine function method. According to Xu et al. [46], the ETrF method produced the smallest RMSE values during the vegetation growing season; then, the study also compared the Gaussian fitting method to the ETrF method. Applying same data described above, daily ET was estimated by the sine function method and the ETrF method. Figure 9 shows the correlations between measurements and estimates acquired by the sine function method (Figure 9(a)) and those retrieved from the ETrF method (Figure 9(b)), respectively. Figure 9 illustrates that both estimates calculated from the sine function method and the ETrF method have good consistency with the measurements, with an R^2 of 0.8, an MAE of 0.58 mm, and an RMSE of 0.67 mm and with an R^2 of 0.82, an MAE of 0.44 mm, and an RMSE of 0.56 mm, respectively. Compared with the Gaussian fitting method, which has an R^2 of 0.82, an MAE of 0.41 mm, and an RMSE of 0.46 mm, daily ET estimates from the sine function method have higher R^2, MAE, and RMSE and estimations by the ETrF method have slightly higher MAE and RMSE, which means the Gaussian fitting method is much appropriate than the sine function method and the ETrF method in estimating the daily ET.

5. Discussion

The Gaussian fitting method applies the Gaussian fitting curve to simulate the diurnal course of ET. Hence, the principle of the method is clear to be understood, and the method is convenient to be utilized. The most obvious advantage of the Gaussian fitting method is that the Gaussian fitting equation has already contained the variable A (the area of curve) which is equal to the daily ET through numerical quadrature. As a result, the acquisition of daily ET is easy. Furthermore, the Gaussian fitting method needs only one time of instantaneous ET retrieved from remote sensing images to estimate daily ET. Compared with the sine function method that is also based on the diurnal course of daytime ET, the Gaussian fitting method requests fewer variables. Therefore, it is much simpler to be used.

The Gaussian fitting method also has some uncertainties. The crucial step in the applications of the Gaussian fitting method is determining the variables w and t_c. However, w is assumed to be equal to half the length of the time during which net radiation is greater than zero, which is totally dependent on the observations. As for t_c, it is highly dependent on the geographic location and its value needs to be adjusted when the study area is different. If there are no ground-based observations for determining variables w and t_c, the Gaussian fitting method would lead to inaccurate daily ET estimates. Therefore, it is necessary to find alternative methods to overcome these issues in the future.

6. Conclusions

Remote sensing is a promising tool to retrieve instantaneous ET on a regional scale. However, the daily ET or a longer timescale ET is more significant to monitor and manage the water resource. Hence, it is essential to convert instantaneous ET into daily ET. The study proposes the Gaussian fitting method to derive daily ET from remotely sensed instantaneous ET. Model validation and application were conducted to test the validity and evaluate the accuracy of the Gaussian fitting method. Model validation showed that the Gaussian fitting curve could well describe the diurnal course of ET measurements at EC stations, with high coefficients of determination and low root mean square errors. As a result, the Gaussian fitting method could be taken as an appropriate approach to simulate daily ET. A case study was performed in the middle reaches of Heihe River, China, to derive daily ET from remotely sensed instantaneous ET. The comparison between daily ET estimates derived by the Gaussian fitting method and measurements obtained from EC stations showed an R^2 of 0.82, an MAE of 0.41 mm, and an RMSE of 0.46 mm, which indicated that the simulated daily ET estimates were quite consistent with the ET measurements and had high accuracy. The frequency distribution of the percent errors also displayed high estimation accuracy, with a variation range of 0%~18%. As for the relationship between daily ET estimates and land cover, the comparison showed that the Gaussian fitting method

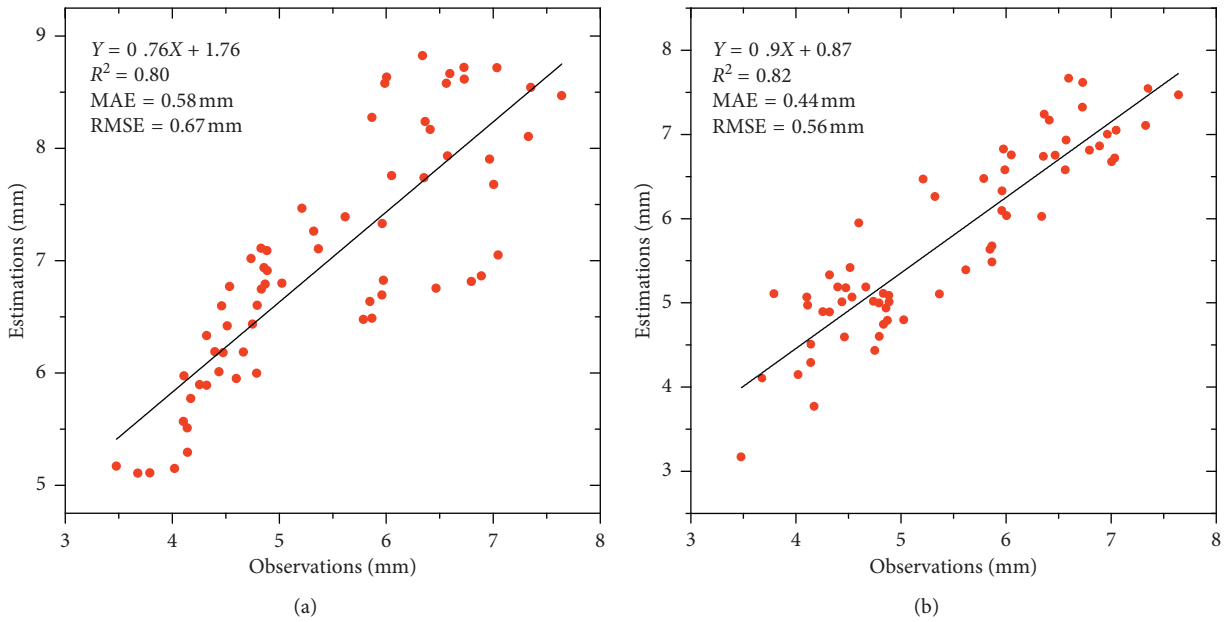

Figure 9: Comparison between daily ET observed by EC stations and that estimated by the sine function method (a) and the ETrF method (b).

could well demonstrate daily ET differences caused by land use types. Estimation error analyses stated that the Gaussian fitting method had higher precision on underlying surfaces covered with vegetation than on bare areas. All analyses conclude that the Gaussian fitting method is efficient and feasible to expand instantaneous ET into daily ET.

Data Availability

The data used in the manuscript include two types, the remote sensing data and the ground-based data. For remote sensing data, the readers can apply for and obtain ASTER images and HJ-1 A/B images through the official websites of USGS (https://glovis.usgs.gov/) and the Satellite Environment Center, Ministry of Environmental Protection of China (http://www.secmep.cn/). Ground-based data were provided by the HiWATER (Heihe Watershed Allied Telemetry Experimental Research) experiment, which was an ecohydrological and watershed-scale experiment in the Heihe River Basin which is the second longest inland river of China. In the paper, we used EC data and automatic meteorological data. Users can apply for the data from Cold and Arid Regions Science Data Center at Lanzhou (http://westdc.westgis.ac.cn/).

Disclosure

An earlier and simpler version of a fraction of this paper has been presented as a conference paper in "Geoscience and Remote Sensing Symposium (IGARSS), 2017 IEEE International."

Conflicts of Interest

The authors declare that there are no conflicts of interest regarding the publication of this paper.

Acknowledgments

This work was supported by the Strategic Priority Research Program of Chinese Academy of Sciences (grant number XDA20010302), the National Natural Science Foundation of China (grant numbers 41571356, 41671368, 41671354, and 41671373), the National Basic Research Program of China (grant number 2013CB733406), the Henan Province University Scientific and Technological Innovation Team (18IRTSTHN009), and the Key Project of National Natural Science Foundation of China (41301363).

References

[1] Z. Kothavala, M. A. Arain, T. A. Black, and D. Verseghy, "The simulation of energy, water vapor and carbon dioxide fluxes over common crops by the Canadian Land Surface Scheme (CLASS)," *Agricultural and Forest Meteorology*, vol. 133, no. 1–4, pp. 89–108, 2005.

[2] M. Anderson, J. Norman, W. Kustas, R. Houborg, P. Starks, and N. Agam, "A thermal-based remote sensing technique for routine mapping of land-surface carbon, water and energy fluxes from field to regional scales," *Remote Sensing of Environment*, vol. 112, no. 12, pp. 4227–4241, 2008.

[3] W. Brutsaert, *Hydrology: An Introduction*, Cambridge University Press, New York, NY, USA, 2005.

[4] C. H. B. Priestley and R. J. Taylor, "On the assessment of surface heat flux and evaporation using large-scale parameters," *Monthly Weather Review*, vol. 100, no. 2, pp. 81–92, 1972.

[5] S. Wang, "Simulation of evapotranspiration and its response to plant water and CO_2 transfer dynamics," *Journal of Hydrometeorology*, vol. 9, no. 3, pp. 426–443, 2008.

[6] W. Abtew and A. Melesse, *Evaporation and Evapotranspiration: Measurements and Estimations*, Springer Netherlands, Dordrecht, The Netherlands, 2013.

[7] E. T. Engman and R. J. Gurney, *Remote Sensing in Hydrology*, Chapman and Hall Ltd., London, UK, 1991.

[8] Y.-A. Liou and S. Kar, "Evapotranspiration estimation with remote sensing and various surface energy balance algorithms—a review," *Energies*, vol. 7, no. 5, pp. 2821–2849, 2014.

[9] P. J. Sellers, R. E. Dickinson, D. A. Randall et al., "Modeling the exchanges of energy, water, and carbon between continents and the atmosphere," *Science*, vol. 275, no. 5299, pp. 502–509, 1997.

[10] E. P. Glenn, A. R. Huete, P. L. Nagler, K. K. Hirschboeck, and P. Brown, "Integrating remote sensing and ground methods to estimate evapotranspiration," *Critical Reviews in Plant Sciences*, vol. 26, no. 3, pp. 139–168, 2007.

[11] W. Kustas and M. Anderson, "Advances in thermal infrared remote sensing for land surface modeling," *Agricultural and Forest Meteorology*, vol. 149, no. 12, pp. 2071–2081, 2009.

[12] W. J. Shuttleworth, "Putting the "vap" into evaporation," *Hydrology and Earth System Sciences*, vol. 11, no. 1, pp. 210–244, 2007.

[13] S. M. Liu, Z. W. Xu, W. Z. Wang et al., "A comparison of eddy-covariance and large aperture scintillometer measurements with respect to the energy balance closure problem," *Hydrology and Earth System Sciences*, vol. 15, no. 4, pp. 1291–1306, 2011.

[14] G. Liu, M. Hafeez, Y. Liu, D. Xu, and C. Vote, "A novel method to convert daytime evapotranspiration into daily evapotranspiration based on variable canopy resistance," *Journal of Hydrology*, vol. 414-415, pp. 278–283, 2012.

[15] K. Wang and R. E. Dickinson, "A review of global terrestrial evapotranspiration: observation, modelling, climatology, and climatic variability," *Reviews of Geophysics*, vol. 50, no. 2, pp. 1–54, 2012.

[16] J. D. Kalma, T. R. McVicar, and M. F. McCabe, "Estimating land surface evaporation: a review of methods using remotely sensed surface temperature data," *Surveys in Geophysics*, vol. 29, no. 4-5, pp. 421–469, 2008.

[17] J. C. B. Hoedjes, A. Chehbouni, F. Jacob, J. Ezzahar, and G. Boulet, "Deriving daily evapotranspiration from remotely sensed instantaneous evaporative fraction over olive orchard in semi-arid Morocco," *Journal of Hydrology*, vol. 354, no. 1–4, pp. 53–64, 2008.

[18] L. Morillas, L. Villagarcía, F. Domingo, H. Nieto, O. Uclés, and M. García, "Environmental factors affecting the accuracy of surface fluxes from a two-source model in Mediterranean drylands: upscaling instantaneous to daytime estimates," *Agricultural and Forest Meteorology*, vol. 189-190, pp. 140–158, 2014.

[19] R. Tang, Z.-L. Li, and X. Sun, "Temporal upscaling of instantaneous evapotranspiration: an intercomparison of four methods using eddy covariance measurements and MODIS data," *Remote Sensing of Environment*, vol. 138, pp. 102–118, 2013.

[20] R. D. Jackson, J. L. Hatfield, R. J. Reginato, S. B. Idso, and P. J. Pinter, "Estimation of daily evapotranspiration from one time-of-day measurements," *Agricultural Water Management*, vol. 7, no. 1–3, pp. 351–362, 1983.

[21] W. Shuttleworth, R. Gurney, A. Hsu, and J. Ormsby, "Remote sensing and large-scale global processes," in *FIFE: the Variation in Energy Partition at Surface Flux Sites*, vol. 186, IAHS Publication, Wallingford, UK, 1989.

[22] I. A. Walter, R. G. Allen, R. Elliott et al., "ASCE's standardized reference evapotranspiration equation," in *Proceedings of Watershed Management and Operations Management 2000*, vol. 40499, pp. 1–11, Fort Collins, CO, USA, June 2000.

[23] L. Zhang and R. Lemeur, "Evaluation of daily evapotranspiration estimates from instantaneous measurements," *Agricultural and Forest Meteorology*, vol. 74, no. 1-2, pp. 139–154, 1995.

[24] T. G. Van Niel, T. R. McVicar, M. L. Roderick, A. I. J. M. van Dijk, L. J. Renzullo, and E. van Gorsel, "Correcting for systematic error in satellite-derived latent heat flux due to assumptions in temporal scaling: assessment from flux tower observations," *Journal of Hydrology*, vol. 409, no. 1-2, pp. 140–148, 2011.

[25] E. Delogu, G. Boulet, A. Olioso et al., "Reconstruction of temporal variations of evapotranspiration using instantaneous estimates at the time of satellite overpass," *Hydrology and Earth System Sciences*, vol. 16, no. 8, pp. 2995–3010, 2012.

[26] M. Sugita and W. Brutsaert, "Daily evaporation over a region from lower boundary-layer profiles measured with radiosondes," *Water Resources Research*, vol. 27, no. 5, pp. 747–752, 1991.

[27] M. Tasumi, R. Trezza, R. G. Allen, and J. L. Wright, "Operational aspects of satellite-based energy balance models for irrigated crops in the semi-arid U.S," *Irrigation and Drainage Systems*, vol. 19, no. 3-4, pp. 355–376, 2005.

[28] R. Trezza, *Evapotranspiration Using a Satellite-Based Surface Energy Balance with Standardized Ground Control*, USU, Logan, UT, USA, 2002.

[29] J. L. Chávez, C. M. U. Neale, J. H. Prueger, and W. P. Kustas, "Daily evapotranspiration estimates from extrapolating instantaneous airborne remote sensing et values," *Irrigation Science*, vol. 27, no. 1, pp. 67–81, 2008.

[30] W. G. M. Bastiaanssen, M. Menenti, R. A. Feddes, and A. A. M. Holtslag, "A remote sensing surface energy balance algorithm for land (SEBAL). 1. Formulation," *Journal of Hydrology*, vol. 212-213, pp. 198–212, 1998.

[31] Z. Su, "The Surface Energy Balance System (SEBS) for estimation of turbulent heat fluxes," *Hydrology and Earth System Sciences*, vol. 6, no. 1, pp. 85–100, 2002.

[32] C. Abdelghani, J. C. B. Hoedjes, J.-C. Rodriquez et al., "Using remotely sensed data to estimate area-averaged daily surface fluxes over a semi-arid mixed agricultural land," *Agricultural and Forest Meteorology*, vol. 148, no. 3, pp. 330–342, 2008.

[33] F. Maselli, D. Papale, M. Chiesi et al., "Operational monitoring of daily evapotranspiration by the combination of MODIS NDVI and ground meteorological data: application and evaluation in Central Italy," *Remote Sensing of Environment*, vol. 152, pp. 279–290, 2014.

[34] S. Liu, H. Su, R. Zhang et al., "A study on deriving daily evapotranspiration from remotely sensed instantaneous evapotranspiration based on the Gaussian fitting method," in *Proceedings of International Geoscience and Remote Sensing Symposium (IGARSS)*, pp. 1923–1926, Fort Worth, TX, USA, July 2017.

[35] A. N. French, F. Jacob, M. C. Anderson et al., "Surface energy fluxes with the advanced spaceborne thermal emission and reflection radiometer (ASTER) at the Iowa 2002 SMACEX site (USA)," *Remote Sensing of Environment*, vol. 99, no. 1-2, pp. 55–65, 2005.

[36] Q. Liu, J. Wen, S. Wu, and Y. Qu, *Albedo Dataset in 30m-Resolution in the Heihe River Basin in 2012*, Heihe Plan Science Data Center, Lanzhou, China, 2014.

[37] H. Li, D. Sun, Y. Yu et al., "Evaluation of the VIIRS and MODIS LST products in an arid area of Northwest China," *Remote Sensing of Environment*, vol. 142, pp. 111–121, 2014.

[38] X. Li, G. Cheng, S. Liu et al., "Heihe watershed allied Telemetry experimental Research (HiWATER): scientific

objectives and experimental design," *Bulletin of the American Meteorological Society*, vol. 94, no. 8, pp. 1145–1160, 2013.

[39] S. Liu, Z. Xu, L. Song et al., "Upscaling evapotranspiration measurements from multi-site to the satellite pixel scale over heterogeneous land surfaces," *Agricultural and Forest Meteorology*, vol. 230-231, pp. 97–113, 2016.

[40] T. Xu, Z. Guo, S. Liu et al., "Evaluating different machine learning methods for upscaling evapotranspiration from flux towers to the regional scale," *Journal of Geophysical Research: Atmospheres*, vol. 123, no. 16, pp. 8674–8690, 2018.

[41] S. Liu, X. Li, Z. Xu et al., "The Heihe integrated observatory network: a basin-scale land surface processes observatory in China," *Vadose Zone Journal*, vol. 17, no. 1, 2018.

[42] Z. Xu, S. Liu, X. Li et al., "Intercomparison of surface energy flux measurement systems used during the HiWATER-MUSOEXE," *Journal of Geophysical Research: Atmospheres*, vol. 118, no. 23, pp. 13,140–13,157, 2013.

[43] R. L. Burden and J. D. Faires, *Numerical Analysis*, Richard Stratton, Boston, MA, USA, 2001.

[44] Y.-C. Wang, T.-Y. Chang, and Y.-A. Liou, "Terrain correction for increasing the evapotranspiration estimation accuracy in a mountainous watershed," *IEEE Geoscience and Remote Sensing Letters*, vol. 7, no. 2, pp. 352–356, 2010.

[45] X. Liu and Y. Bo, "Object-based crop species classification based on the combination of airborne hyperspectral images and LiDAR data," *Remote Sensing*, vol. 7, no. 1, pp. 922–950, 2015.

[46] T. Xu, S. Liu, L. Xu et al., "Temporal upscaling and reconstruction of thermal remotely sensed instantaneous evapotranspiration," *Remote Sensing*, vol. 7, no. 3, pp. 3400–3425, 2015.